Determination of complex optical constants and photovoltaic device design of all-inorganic CsPbBr₃ perovskite thin films

WENSHENG YAN,[1,4] LINGYUN MAO,[2] PEIYANG ZHAO,[2] ADRIAN MERTENS,[1,3] STEPHAN DOTTERMUSCH,[1] HANG HU,[1] ZHONG JIN,[2,5] AND BRYCE S. RICHARDS[1,3]

[1]*Institute of Microstructure Technology (IMT), Karlsruhe Institute of Technology, Hermann-von-Helmholtz-Platz 1, 76344 Eggenstein-Leopoldshafen, Germany*
[2]*Key Laboratory of Mesoscopic Chemistry of MOE, Jiangsu Key Laboratory of Advanced Organic Materials, School of Chemistry and Chemical Engineering, Nanjing University, Nanjing 210023, China*
[3]*Light Technology Institute (LTI), Karlsruhe Institute of Technology, Engesserstrasse 13, 76131 Karlsruhe, Germany*
[4]*Wensheng.Yan@kit.edu*
[5]*Zhongjin@nju.edu.cn*

Abstract: All-inorganic perovskites exhibit interesting properties and unprecedented stability compared to organic-inorganic hybrid lead halide perovskites. This work focuses on depositing and characterizing cesium lead bromide (CsPbBr₃) thin films and determining their complex optical constants, which is a key requirement for photovoltaic device design. CsPbBr₃ thin films are synthesized via the solution method followed by a hot-embossing step to reduce surface roughness. Variable angle spectroscopic ellipsometry measurements are then conducted at three angles (45°, 55°, and 65°) to obtain the ellipsometric parameters psi (Ψ) and delta ($\varDelta$). For the present model, bulk planar CsPbBr₃ layer is described by a one-dimensional graded index model combined with the mixture of one Tauc-Lorentz oscillator and two Gaussian oscillators, while an effective medium approximation with 50% air void is adopted to describe surface roughness layer. The experimental complex optical constants are finally determined in the wavelength range of 300 to 1100 nm. Furthermore, as a design example demonstration, the simulations of single-junction CsPbBr₃ solar cells are conducted via the finite-difference time-domain method to investigate the properties of light absorption and photocurrent density.

1. Introduction

Since the first perovskite solar cell (PSC) was reported in 2009 [1], a massive research effort has been underway. The power conversion efficiency (PCE) of the organic-inorganic hybrid PSCs based on lead halides progressed rapidly from 3.8% to a certificated record efficiency of 24.2% [1,2]. PSCs are especially promising due to their unique properties such as excellent light absorption and long charge carrier diffusion lengths, while devices can be deposited using facile and low-cost fabrication techniques. Up to now, a key challenge confronting PSCs is their poor stability against humidity, heat, and UV light, which is delaying their appearance in the marketplace [3].

Recently, all-inorganic cesium lead bromide (CsPbBr₃) PSCs have attracted significant attention due to their greatly improved stability [4–6]. To date, several groups have demonstrated excellent stability of CsPbBr₃ PSCs against humidity and heat when compared with conventional organic-inorganic hybrid PSCs [7–9]. However, improving the PCE of the all-inorganic devices is still a primary concern [10–13]. As such, optical simulations are definitely helpful to not only physical

understandings on light interaction with the material, but also for investigating different solar cell architectures.

To implement the above optical simulations and device designs, the knowledge of complex optical constants of $CsPbBr_3$ thin films is mandatory. In the area of organic-inorganic hybrid perovskites, there are already many reports regarding determination of the optical constants [14–18]. In contrast, the reports on the refractive index (n) and extinction coefficient (k) of all-inorganic perovskite thin films are rare [19,20]. In the work by Zhao *et al.* it is noted that a high root-mean-square (RMS) surface roughness of 37.4 nm of the $CsPbBr_3$ films could result in an underestimation of the refractive index values ($n = 1.93$ at 525 nm) [19]. A further limitation is that the ellipsometry measurements were conducted only at one angle of incidence (75°). Therefore, it was deemed pertinent to undertake the necessary investigations and to determine how these values for the optical constants might vary for a sample with low surface roughness and also when the ellipsometric measurements are taken at three angles of incidence. This would give more confidence in the extracted n and k values, which are then to be employed in optical simulations to explore different photovoltaic device designs based on the $CsPbBr_3$ absorber. Previously, the given wavelength range of the optical constants of the $CsPbBr_3$ was from 300 to 800 nm in Ref. [19]. Extending the wavelength of the complex optical constants to 1100 nm can offer an opportunity to design and simulate high-efficiency $CsPbBr_3$/crystalline silicon (c-Si) tandem solar cells.

In the present work, the $CsPbBr_3$ thin films are synthesized via the solution method, followed by a hot-embossing step in order to reduce the RMS surface roughness to 9 nm. The complex optical constants of the $CsPbBr_3$ thin films are determined via variable angle spectroscopic ellipsometry (VASE) measurements, which are conducted at three angles (45°, 55°, and 65°) for obtaining the two ellipsometric data, psi (Ψ) and delta (Δ). In order to achieve the excellent fitting with the measured Ψ and Δ, it is of critical importance to construct a proper model. Here, one-dimensional graded-index model through the film from bottom to up combined with the mixture of one Tauc-Lorentz (T-L) oscillator and two Gaussian (Gau) oscillators are adopted to describe bulk $CsPbBr_3$ layer while an effective medium approximation (EMA) model with 50% air void is chosen to describe surface roughness layer. As a result, the complex optical constants of the $CsPbBr_3$ thin films are experimentally determined in the wavelength range of 300 to 1100 nm. Our model for extracting optical constants of $CsPbBr_3$ is different from the model of Zhao *et al.*, where they adopted seven T-L oscillators and the front rough $CsPbBr_3$ surficial layer was not included. It was also noted that they actually obtained 'pseudo' optical constants [19]. Subsequently, as an example demonstration, our obtained n and k values are used to investigate the light absorption and photocurrent density (J_{sc}) of a single-junction $CsPbBr_3$ solar cell via the finite-difference time-domain (FDTD) simulations.

2. Methods

2.1. Experiments

In this study, all the fabrication steps of $CsPbBr_3$-based inorganic perovskite thin films are conducted in ambient air and without humidity control (about 25°C and 60% relative humidity). $CsPbBr_3$ thin film is deposited on the rear of fluorine-doped tin oxide (FTO) thin film coated glass substrates and as a result, the sample structure consists of $CsPbBr_3$ thin film/glass substrate/FTO thin film. In terms of sample preparation process, the glass/FTO is sequentially ultrasonic cleaned with acetone, ethanol and pure water. Then, a N,N-dimethylformamide (DMF) solution of 1.0 M $PbBr_2$ is spin-coated onto the glass side at 2000-3500 rpm for 30 s to yield a precursor solution. The prepared film is then dipped in a methanol solution of 0.07 M CsBr for 10 min, rinsed with isopropanol, dried by spin in air, and heated to 250 °C for 5 min on a hotplate to form a uniform layer of $CsPbBr_3$. More details refer to Ref. [7]. When the preparations of the $CsPbBr_3$ thin films are finished, the FTO thin film layer is mechanically removed from the glass substrate with

the result of rough rear surface to enable more accurate ellipsometric measurements. It should be noted that although FTO-coated substrates were used in this work, this is not important as even if the CsPbBr$_3$ thin film has been deposited on a bare glass substrate, the rear side would still need to be mechanically roughened rear before VASE experiments and analysis.

The pressing of CsPbBr$_3$ thin films is conducted using an in-house hot-embossing machine [21–23]. The sample for hot embossing is placed between the upper and lower stainless steel plates and the substrate can be heated up. In this work, the sample size is $2\,cm \times 2\,cm$. A polished silicon wafer is used as a mold in order to achieve a smooth CsPbBr$_3$ surface with low surface roughness. To compare difference between the hot-embossed and non-embossed regions of the sample, the mold size is smaller than the size of the sample. A force of 30000 N is applied for the present experiment. It is necessary to point out that too large force can break the sample while too small force is not effective in significantly reducing the surface roughness. The present hot embossing of CsPbBr$_3$ film referred to a previous report on a perovskite Cs$_{0.1}$(MA$_{0.17}$FA$_{0.83}$)$_{0.9}$Pb(I$_{0.83}$Br$_{0.17}$)$_3$ thin film [23]. We found that the substrate temperature of 60 °C can significantly decrease the surface roughness from 35 nm to 9 nm for CsPbBr$_3$ thin film, which is good enough to achieve the purpose of this work for experimental determination on the complex optical constants of the CsPbBr$_3$ thin films. The mold pressing time is 20 min. When the hot embossing is finished, the sample is left to cool down to room temperature and then is demolded.

2.2. Characterization

X-ray diffraction (XRD) spectra are collected with a diffractometer (Bruker D-8 Advance) using Cu $K\alpha$ X-ray radiation to investigate the crystalline structure. The wavelength dependent transmission and absorption of the sample are conducted by using a spectrophotometer equipped with an integrating sphere (Perkin Elmer Lambda 950). The photoluminescence (PL) spectrum is measured (Hitachi F-4600) to compare with the bandgap of the CsPbBr$_3$ obtained from the Tauc plot method. Scanning electron microscopy (SEM, Zeiss Supra 60VP) images are obtained in order to assess the surface morphology and film thickness. An atomic force microscope (AFM, Bruker Dimension Icon) is used to investigate surface roughness of the samples. A VASE (M-2000 F, J. A. Woollam Co. Inc) is the main tool used to measure ellipsometry output data (Ψ and Δ), with measurements conducted at three angles: 45°, 55°, and 65°. The estimated diameter of beam spot used in the present ellipsometry measurements at the three angles is 1.5-2 mm. Besides, the Sentech spectroscopic ellipsometry instrument (Model: SENresearch 4.0, Germany) is also used to assess the measurement uncertainty of the optical constants, where the beam spot size is 2-4 mm. The adopted models for the fitting to the ellipsometric data are the same between the two instrument measurements.

2.3. WVASE model and photocurrent density simulations

In order to determine the n and k of the CsPbBr$_3$ thin film, a commercial software package (WVASE32 v.3.888, J. A. Woollam) is employed to construct a proper model to fit the ellipsometric data Ψ and Δ. As we know, an ideal thin film that is homogenous and exhibits perfectly flat surfaces rarely occurs in the real world. The most commonly encountered cases are non-ideal thin film such as surface roughness at the top, thickness variation, and a variation of the optical constants from top to bottom throughout the film [24].

The ellipsometric parameters Ψ and Δ can be related to the ratio of Fresnel reflection coefficients R_p and R_s for p- and s-polarized light as described in Eq. (1) :

$$\rho = \frac{R_p}{R_s} = \tan(\psi)e^{i\Delta} \tag{1}$$

The VASE technique measures the ratio of the two values and as a result, the measured results are highly accurate and reproducible [24]. For the present sample (CsPbBr$_3$ perovskite thin film on a glass substrate), the Cauchy dispersion function is used to describe the property of the glass substrate. In the model for the CsPbBr$_3$ layer, the perovskite thin film is divided into (or equivalent to) two parts. The one is bulk planar perovskite layer (the bulk thickness is defined as d_{bulk}). The other is a surface roughness layer consisting of the mixture of air void and perovskite material (vertical surface roughness of this layer is defined as d_{rough}). To illustrate this model, a drawing of the CsPbBr$_3$ layer is shown in Fig. 4(a). For the surface roughness layer, a Bruggeman effective medium approximation (EMA) is usually suitable, whereby the medium consists of the mixture of x% air void and $(100 - x)$% perovskite material, where x can take a value in the range from 0 to 100. For bulk perovskite layer (d_{bulk}), the oscillators such as Tauc-Lorentz (T-L) and Gaussian (Gau) were successfully used to describe the dielectric function of the perovskites [14–18]. The T-L oscillator function and Gau oscillator function are expressed in Eq. (2) - Eq. (4), respectively [24]:

$$\varepsilon_{n\_T-L} = \varepsilon_{n1} + i\varepsilon_{n2} \tag{2}$$

where, when $E \leq Eg_n$, $\varepsilon_{n2} = 0$; when $E > Eg_n$,

$$\varepsilon_{n2} = \left[\frac{A_n Eo_n C_n (E - Eg_n)^2}{(E^2 - Eo_n^2)^2 + C_n^2 E^2} \times \frac{1}{E} \right] \tag{3}$$

In Eqs. (2) and (3), the subscript T-L indicates that the model is based on the Tauc joint density of states and the Lorentz oscillator. These four fitting parameters are A_n, Eo_n, C_n, and Eg_n, where these parameters are in units of energy of eV.

$$\varepsilon_{n\_Gau} = \varepsilon_{n1} + i\varepsilon_{n2} \tag{4}$$

where,

$$\varepsilon_{n1} = \frac{2}{\pi} P \int_0^\infty \frac{\xi \varepsilon_{n2}(\xi)}{\xi^2 - E^2} d\xi$$

$$\varepsilon_{n2} = A_n^{-\left(\frac{E-E_n}{\sigma}\right)^2} - A_n^{-\left(\frac{E+E_n}{\sigma}\right)^2}$$

$$\sigma = \frac{Br_n}{2\sqrt{\ln(2)}}$$

In Eq. (4), the subscript Gau indicates that the model is based on the Gaussian oscillator. The three fitting parameters that are used for the WVASE fitting are A_n, where the unit is dimensionless, E_n, where the unit is eV, and Br_n, where the unit is eV.

Several studies have pointed out that variation of the optical constants of a thin film along the direction normal to the film (i.e. vertically through the film) is most commonly caused by the drifting of process parameters during the deposition of the film or induced by post-deposition processing of the film such as annealing [24]. In the preparation of the present CsPbBr$_3$ thin films, a two-step deposition was used, where a heating at 250 °C for 5 min was involved. Furthermore, the sample was heated at 60 °C for 20 min during the hot embossing, which can be regarded as a low temperature annealing. These facts suggest that the model of one-dimensional graded index along the direction normal to the film could be considered. Graded layers work by creating a series of homogenous layers with optical constants that change slightly in each layer.

Regarding the calculation of light absorption and J_{sc} of the CsPbBr$_3$ solar cells, the light absorption power, P_{abs}, is calculated from the divergence of the Poynting vector using the

following equation:

$$P_{abs} = 0.5\omega\varepsilon_{im}|E(\omega)|^2 \tag{5}$$

where ω is the angular frequency, ε_{im} is the imaginary part of the permittivity, and E is the electric field. During the present simulations, the normalized light absorptivity in the perovskite absorber can be determined by:

$$A(\lambda) = P_{abs}(\lambda)/P_{in}(\lambda) \tag{6}$$

where $P_{in}(\lambda)$ is the power of incident light within the solar cell at a wavelength λ. Here, we assume that all generated electron-hole pairs are extracted and collected – in other words, a unity quantum efficiency – such that the J_{sc} can be calculated by integrating light absorption $A(\lambda)$ over all wavelengths as follows:

$$J_{sc} = e \int \lambda/hc \times A(\lambda)I_{AM1.5}(\lambda)d\lambda \tag{7}$$

where, e is the charge of an electron in the unit of C. h is Plank's constant in the unit of J·s. c is the speed of light in free space with the unit of m/s, and $A(\lambda)$ is the light absorption as function of wavelength. $I_{AM1.5}$ is air mass 1.5 global solar spectrum with unit of W/m^2/nm.

3. Results and discussion

The measured XRD pattern of the as-prepared CsPbBr$_3$ thin film on the bare glass substrate is shown in Fig. 1(a), where the inset is a photo of the sample and a standard XRD pattern of a cubic CsPbBr$_3$ is cited from Ref. [25]. The XRD result indicates that the crystal structure of CsPbBr$_3$ is in a cubic (*Pm3 m*) phase and falls within a standard XRD pattern reported for a cubic CsPbBr$_3$ phase [25]. However, it is noted that compared with the standard pattern, some of small peaks are not detected as they are too weak, as is also sometimes reported in the literature [6,7,25,26]. After hot embossing of the CsPbBr$_3$ thin film at 60 °C, the crystalline structure remains unchanged. By using a Tauc plot for the measured wavelength-dependent transmission of the hot-embossed CsPbBr$_3$ thin film (~400 nm thickness) in the wavelength range of 300 to 1100 nm, the optical bandgap is estimated from the plotting of $(Ah\nu)^2$ versus photon energy ($h\nu$) as shown in Fig. 1(b). It is found that the present CsPbBr$_3$ perovskite film exhibits a direct bandgap of 2.3 eV, consistent with previous reports [7,9,27]. The PL spectrum of CsPbBr$_3$ thin film is measured and shown in Fig. 1(b). The obtained bandgap is 2.3 eV, which is consistent
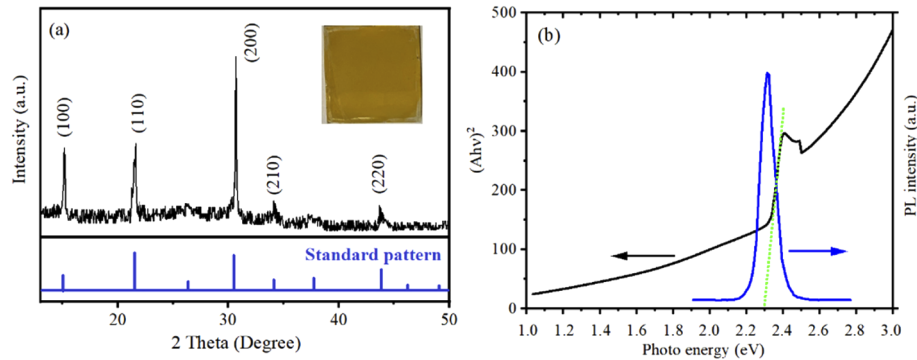

Fig. 1. (a) XRD pattern of the present CsPbBr$_3$ thin film on glass substrate, where the inset is a sample photo and a standard XRD pattern of a cubic CsPbBr$_3$ is included. (b) Tauc plot of *(Ah\nu)*^{2} versus photon energy (*h\nu*) in order to estimate the optical bandgap (green dotted line), which is confirmed via the PL spectrum.

with the bandgap determined from the Tauc-plot method. Specifically, via the Tauc-plot method, the obtained bandgap is 540 nm, while from PL measurements the peak is at 537 nm.

Top-view SEM morphologies of the $CsPbBr_3$ thin film at two different magnifications are shown in Figs. 2(a) and 2(b). The morphology difference between hot embossed and non-embossed regions are clearly visible, with the top half of the image region has no hot embossing and bottom half region has hot embossing. It is clearly seen in both Figs. 2(a) and 2(b) that the smooth degree of the $CsPbBr_3$ surface has been obviously improved by the hot embossing. This indicates that hot embossing can significantly reduce the degree of surface roughness. Figure 2(c) shows a cross-section image of the hot-embossed $CsPbBr_3$ thin film and the estimated thickness is 395 nm. To assess the surface roughness of the interested embossed region, a measured three-dimensional (3D) AFM image is shown in Fig. 3. The RMS surface roughness value is 9 nm for the hot-embossed region, while for the non-embossed region the average RMS roughness is ~35 nm. It should be pointed out that the RMS surface roughness of 9 nm as shown in Fig. 3 is for a single measurement. We have made roughness measurements at different regions and the variation is ± 2 nm.
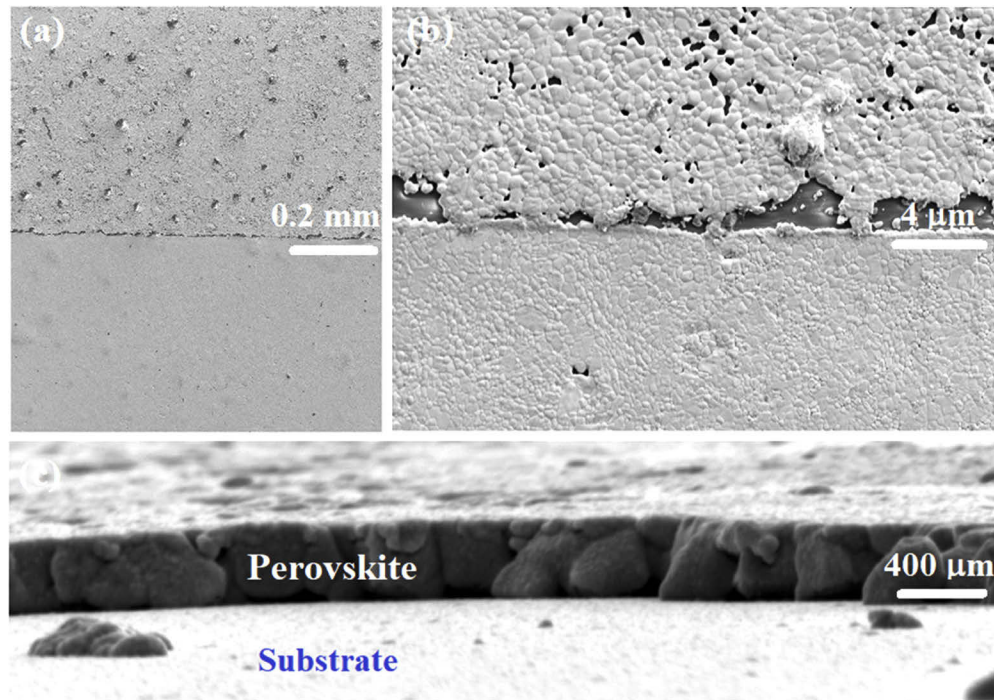

Fig. 2. (a) Top-view SEM image of the $CsPbBr_3$ thin film, where top half region has no hot embossing and bottom half region has hot embossing. (b) A higher magnification SEM image of the $CsPbBr_3$ thin film. (c) Cross-sectional SEM image of the embossed $CsPbBr_3$ thin film.

Figure 4(a) shows a schematic of a perovskite $CsPbBr_3$ thin film on a bare glass substrate. Figure 4(b) is the established model to fit the measured Ψ and Δ, where an EMA model with 50% of air void is used to describe rough $CsPbBr_3$ surface; one-dimensional graded-index model through the film from bottom to top combined with one T-L oscillator and two Gau oscillators are used to describe the bulk flat $CsPbBr_3$ layer; The Cauchy dispersion model is used to describe the glass substrate, where it is a soda-lime glass. The measured and fitted Ψ and Δ at the angles of 45°, 55°, and 65° are presented in Figs. 4(c) and 4(d) in the wavelength range of 300 to
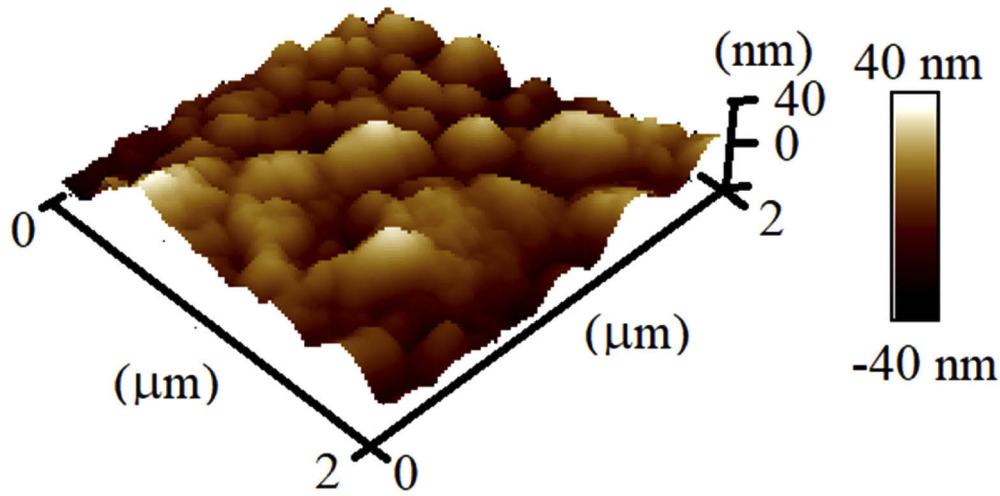
Fig. 3. AFM images of the hot-embossed CsPbBr$_3$ thin film with the size of 2 μm by 2 μm in 3D view.

1100 nm, respectively. It can be seen that very good fitting results are achieved for both Ψ and Δ. Via the optimization, it is found the best fitting results are as follows: a graded index variation of 11% from the bottom to top through the perovskite thin film; one T-L oscillator and two Gau oscillators; thicknesses of the bulk perovskite layer and the surface roughness extracted from the fitting results are 402 nm and 10 nm, respectively, which are both in close agreement with the SEM and AFM results. Finally, the extracted parameters from the best fitting and the estimated values from the measurements are summarized in Table 1. It is further found that if either the graded index model was not included or all oscillators fully adopts T-L oscillators, the fitting results are worsened causing serious deviation of the optical constants. In contrast, if all oscillators adopts Gau oscillators, the optical constants are affected slightly.

Table 1. The extracted parameters from the best fitting using M-2000 F (J. A. Woollam Co. Inc) and the experimental estimation.

Oscillators	A$_n$	E$_n$ or Eo$_n$ (eV)	C$_n$	Eg$_n$ (eV)	Br$_n$ (eV)
1: T-L	295.6 (eV)	2.42	0.035	2.60	
2: Gau	0.95	2.40			0.07
3: Gau	5.75	5.43			2.71
d$_{rough}$:	10 nm (VASE result)		9 ± 2 nm (AFM result)		
d$_{bulk}$:	403 nm (VASE result)		395 ± 10 nm (SEM result)		
Refractive index variation: 11% (fitting result)					

From the above best fitting results, we can obtain the dispersive *n* and *k* values. Their results are shown in Fig. 5 using solid lines, where the reported optical constants of a CsPbBr$_3$ thin film in the wavelength range of 300-800 nm are cited from Ref. [19] for comparison and discussion. On the one hand, compared with Ref. [19], the overall trends in *n* and *k* values are similar in the wavelength range of 300 to 800 nm. On the other hand, our *n* values are obviously higher than that of the report in this wavelength range. In addition, we extend the complex optical constants to longer wavelength of 1100 nm, which offers a unique opportunity to do design and simulations on high-efficiency CsPbBr$_3$/c-Si tandem solar cells. It was noted that a high RMS surface roughness of 37 nm could result in an underestimation of the refractive index (*n* = 1.93 at about 525 nm)
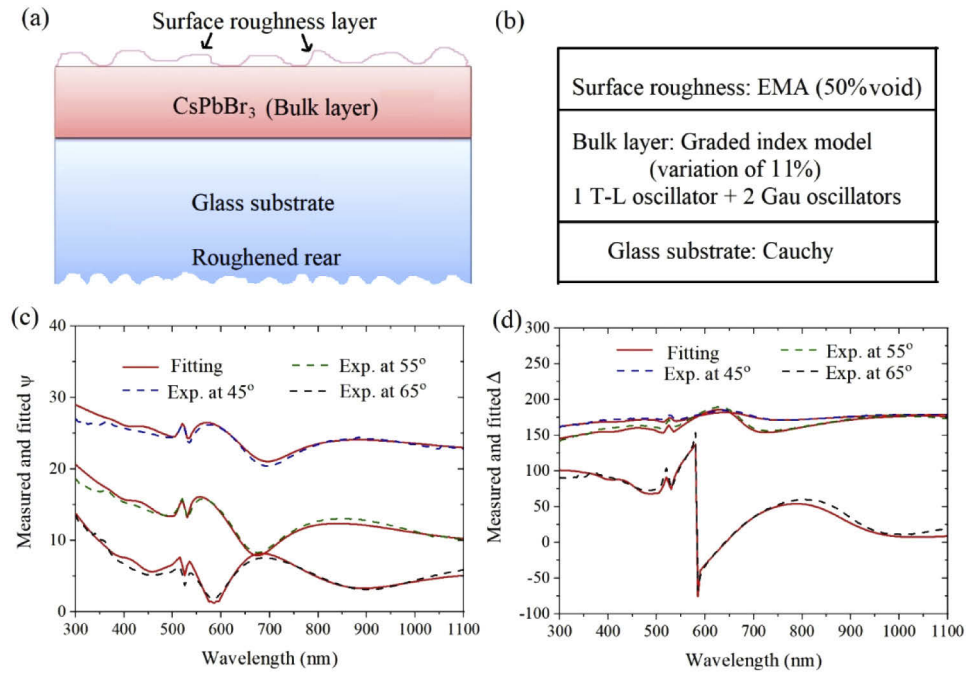
Fig. 4. (a) Schematic diagram of the present sample structure consisting of perovskite CsPbBr$_3$ thin film on glass substrate with the roughened rear surface. (b) Established model for the present fitting. (c) The measured and fitted Ψ at the three angles of 45°, 55°, and 65° in the wavelength range of 300 to 1100 nm. (d) The measured and fitted Δ at the angles of 45°, 55°, and 65° in the wavelength range of 300 to 1100 nm.

values [19]. It is found that at the wavelength of 525 nm, the *n* value obtained from this work is 2.12, which indicates that our *n* value is 10% larger than the report at this wavelength. Regarding a comparison of *k* values, one main difference is that in the present work, the *k* values approach zero for wavelengths greater than 550 nm whereas the *k* values in the report remain at around 0.11. The k values being zero at longer wavelengths means that the CsPbBr$_3$ thin film becomes non-absorptive. Thus, it is suitable to develop high-efficiency CsPbBr$_3$/c-Si tandem solar cells, which are based on the working principle that top semi-transparent perovskite cell and bottom c-Si solar cell can absorb the shorter (300-550 nm) and longer (550-1100 nm) wavelengths of sunlight, respectively. In this way, such tandem solar cell (for example, a four-terminal device) has the potential to produce a power conversion efficiency exceeding the Shockley-Queisser limit. To assess the uncertainty of the optical constants of the CsPbBr$_3$ thin films, the ellipsometric measurements are conducted on both different regions of a single sample and on different samples, where the assessments are extended to include a different ellipsometry instrument (Sentech) as well. For the measurements on the two instrument, the beam spot sizes are different as described in the characterization section and the adopted models are the same for the ellipsometric fitting. The results of the uncertainty are shown in Fig. 5 using shadow bands, where the solid lines are for the best result based on J. A. Woollam instrument and the shadow bands are the uncertainty for all results based on the two instruments. It is found that the variation of the obtained optical constants of CsPbBr$_3$ is less than 3% compared with the result of Fig. 5 in solid lines. To further check the validity of the obtained optical constants, the comparison of transmission and reflection between the measurements and simulations in the wavelength range of 300 to 1100 nm is plotted in Fig. 6. It can be seen that good agreement between the measurement and calculated

spectrophotometric data is achieved, thus giving further confidence to the *n* and *k* values extracted from VASE measurements.
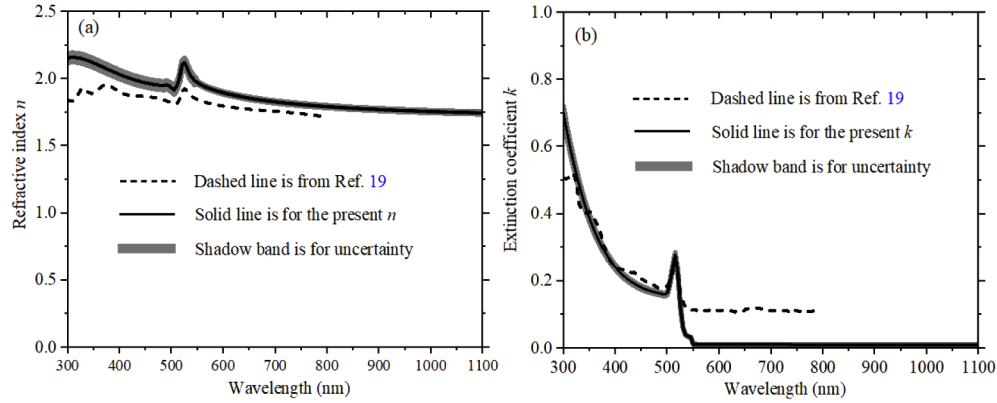

Fig. 5. (a)The determined refractive index (*n*) of the CsPbBr$_3$ thin film in the wavelength range of 300 to 1100 nm as shown in solid line, where the measurement uncertainty is shown using shadow band. For comparison, a report regarding complex optical constants of a CsPbBr$_3$ thin film in the wavelength rang of 300 to 800 nm is cited as shown in dashed lines. (b) The obtained extinction coefficient (*k*) result, measurement uncertainty, and the comparison with Ref. [19].
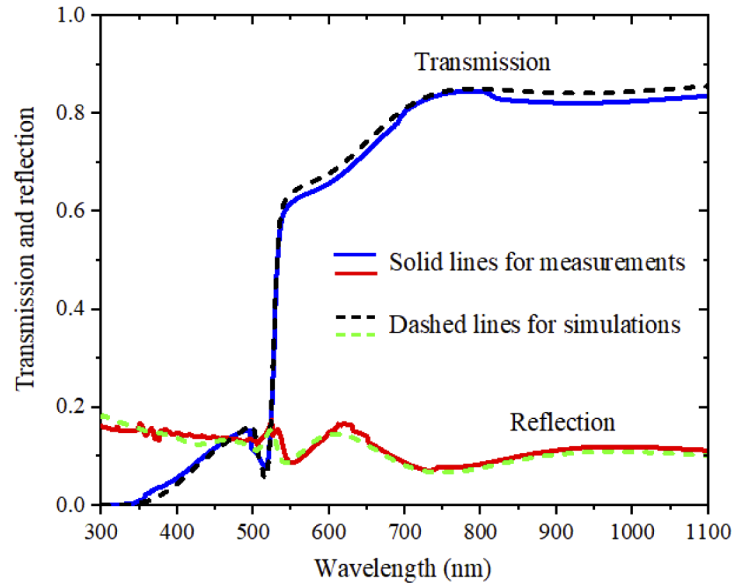

Fig. 6. The measured and simulated transmission and reflection in the wavelength range of 300 to 1100 nm, where solid lines are for measurements and dashed lines are for simulations.

Once the complex optical constants of CsPbBr$_3$ thin films are obtained, the photovoltaic (PV) device design can be conducted via the FDTD simulations. The optical constants of other required materials are well established and can be taken from literature. In the present work, as an example demonstration, we focus on single-junction CsPbBr$_3$ solar cells to conduct investigations on the light absorption and J_{sc}. Because the CsPbBr$_3$ thin films have the optical bandgap of 2.3 eV,

the spectral response range of the PV application of the CsPbBr$_3$ solar cells is from 300 nm to around 540 nm. It is confirmed by a PV device report, where when the wavelengths are greater than 540 nm, the external quantum efficiency (EQE) of the CsPbBr$_3$ solar cells becomes zero [9]. It means that to investigate light absorption and photocurrent density of the single-junction CsPbBr$_3$ solar cells (2.3 eV bandgap) for PV application, it is fair and sufficient to limit the wavelength range to 300-540 nm.

The constructed CsPbBr$_3$ solar cell schematic is shown in Fig. 7(a), where the absorber thicknesses are varied from 100 to 500 nm with an interval of 100 nm to investigate the effect of the absorber thickness on the light absorption and J_{sc}. The thicknesses of FTO, titanium dioxide (TiO$_2$), 2,2',7,7'-Tetrakis[N,N-di(4-methoxyphenyl)amino]-9,9'-spirobifluorene (Spiro-OMeTAD), and gold (Au) layers are set as 400 nm, 50 nm, 50 nm, and 300 nm, respectively. Correspondingly, the complex optical constants of FTO, TiO$_2$, and Spiro-OMeTAD for simulations are cited from the reported measurements [28] and the optical constants of Au and soda lime glass are taken from the literature [29]. In the present simulations, the soda lime glass substrate is included with the thickness of 2 mm, where complex optical constants are taken from the literature [30]. The calculated J_{sc} as a function of the absorber thickness is shown in Fig. 7(a). It is seen that the J_{sc} increases with the absorber thickness. When the absorber thickness is 100 nm, the J_{sc} value is as low as 2.4 mA/cm^2. When the absorber thickness increases from 100 nm to 300 nm, the J_{sc} increases significantly from 2.4 to 5.6 mA/cm^2 with an enhancement of 2.3 times, which can be understood from the calculated light absorption as shown in Fig. 7(b). It can be seen in Fig. 7(b) that compared to the light absorption of 100 nm-thick absorber, the absorption in the 200 nm- and 300 nm-thick absorbers presents a whole broadband light absorption enhancement in the wavelength range of around 350-540 nm. In contrast, as shown in Fig. 7(a), the J_{sc} presents a small increase when the absorber thicknesses are further increased from 300 nm to 500 nm. Specifically, the photocurrent density values are 5.8 and 6.2 mA/cm^2 for the absorber thicknesses of 400 nm and 500 nm, respectively. This indicates that the absorber thickness should be 300 nm at least to acquire a good light absorption. It is noted in Fig. 7(b) that the calculated light absorption at the wavelength of 540 nm is not zero, which is because the obtained extinction coefficient k value does not exactly reach zero at this wavelength. However, its effect on the calculated J_{sc} values is so small that can be neglected.
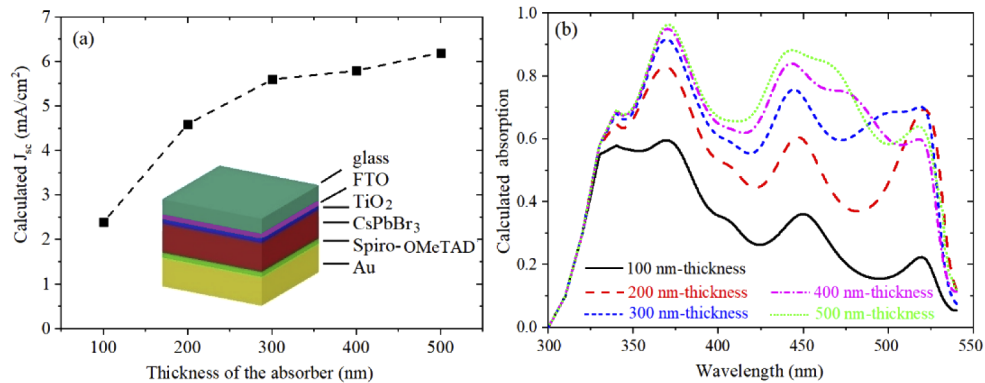

Fig. 7. (a) Calculated J_{sc} values of the CsPbBr$_3$ cells with the absorber thickness varying from 100 to 500 nm with an interval of 100 nm. (b) Calculated absorption in the CsPbBr$_3$ absorbers versus wavelength.

4. Conclusions

The complex optical constants of the CsPbBr$_3$ thin films were determined via the VASE measurements at three variable angles for the hot-embossed CsPbBr$_3$ thin films and the constructed model, where one-dimensional simple graded-index model and the EMA model with 50% air void were used to describe bulk perovskite and rough surface. The transmission and reflectance between the measurement and simulation show a good agreement. The obtained optical constants enable to implement the design and simulations of the CsPbBr$_3$ based PV device. As a representative example demonstration, the photocurrent densities were investigated for single-junction CsPbBr$_3$ solar cells with varying absorber thickness, which can be understood from the calculated wavelength dependent light absorption. These results enable to help to improve the efficiency of single-junction CsPbBr$_3$ solar cells and develop high-efficiency CsPbBr$_3$/c-Si tandem solar cells via the design and simulations.

Disclosures

The authors declare that there are no conflicts of interest related to this article.

References

1. A. Kojima, K. Teshima, Y. Shirai, and T. Miyasaka, "Organometal halide perovskites as visible-light sensitizers for photovoltaic cells," J. Am. Chem. Soc. **131**(17), 6050–6051 (2009).
2. NREL, Best research-cell efficiency chart, https://www.nrel.gov/pv/cell-efficiency.html, access on April 17, 2019.
3. Y. G. Rong, Y. Hu, A. Y. Mei, H. R. Tan, M. I. Saidaminov, S. Seok, M. D. McGehee, E. H. Sargent, and H. W. Han, "Challenges for commercializing perovskite solar cells," Science **361**(6408), eaat8235 (2018).
4. M. Kulbak, D. Cahen, and G. Hodes, "How important is the organic part of lead halide perovskite photovoltaic cells? efficient CsPbBr$_3$ cells," J. Phys. Chem. Lett. **6**(13), 2452–2456 (2015).
5. R. J. Sutton, G. E. Eperon, L. Miranda, E. S. Parrott, B. A. Kamino, J. B. Patel, M. T. Hörantner, M. B. Johnston, A. A. Haghighirad, D. T. Moore, and H. J. Snaith, "Bandgap-tunable cesium lead halide perovskites with high thermal stability for efficient solar cells," Adv. Energy Mater. **6**(8), 1502458 (2016).
6. R. E. Beal, D. J. Slotcavage, T. Leijtens, A. R. Bowring, R. A. Belisle, W. H. Nguyen, G. F. Burkhard, E. T. Hoke, and M. D. McGehee, "Cesium lead halide perovskites with improved stability for tandem solar cells," J. Phys. Chem. Lett. **7**(5), 746–751 (2016).
7. J. Liang, C. Wang, Y. Wang, Z. Xu, Z. Lu, Y. Ma, H. Zhu, Y. Hu, C. Xiao, X. Yi, G. Zhu, H. Lv, L. Ma, T. Chen, Z. Tie, Z. Jin, and J. Liu, "All-inorganic perovskite solar cells," J. Am. Chem. Soc. **138**(49), 15829–15832 (2016).
8. M. Kulbak, S. Gupta, N. Kedem, I. Levine, T. Bendikov, G. Hodes, and D. Cahen, "Cesium enhances long-term stability of lead bromide perovskite-based dolar cells," J. Phys. Chem. Lett. **7**(1), 167–172 (2016).
9. K. C. Tang, P. You, and F. Yan, "Highly stable all-inorganic perovskite solar cells processed at low temperature," Sol. RRL **2**(8), 1800075 (2018).
10. J. Lei, F. Gao, H. X. Wang, J. Li, J. X. Jiang, X. Wu, R. R. Gao, Z. Yang, and S. Z. (Frank) Liu, "Efficient planar CsPbBr$_3$ perovskite solar cells by dual-source vacuum evaporation," Sol. Energy Mater. Sol. Cells **187**, 1–8 (2018).

11. H. W. Yuan, Y. Y. Zhao, J. L. Duan, Y. D. Wang, X. Y. Yang, and Q. W. Tang, "All-inorganic CsPbBr$_3$ perovskite solar cell with 10.26% efficiency by spectra engineering," J. Mater. Chem. A **6**(47), 24324–24329 (2018).

12. X. Y. Liu, X. H. Tan, Z. Y. Liu, H. B. Ye, B. Sun, T. L. Shi, Z. R. Tang, and G. L. Liao, "Boosting the efficiency of carbon-based planar CsPbBr$_3$ perovskite solar cells by a modified multistep spin-coating technique and interface engineering," Nano Energy **56**, 184–195 (2019).

13. Y. Y. Zhao, T. S. Liu, F. M. Ren, J. L. Duan, Y. D. Wang, X. Y. Yang, Q. H. Li, and Q. W. Tang, "Organic hole-transporting materials for 9.32%-efficiency and stable CsPbBr$_3$ perovskite solar cells," Mater. Chem. Front. **2**(12), 2239–2244 (2018).

14. P. Löper, M. Stuckelberger, B. Niesen, J. Werner, M. Filipič, S.-J. Moon, J.-H. Yum, M. Topič, S. De Wolf, and C. Ballif, "Complex refractive index spectra of CH$_3$NH$_3$PbI$_3$ perovskite thin films determined by spectroscopic ellipsometry and spectrophotometry," J. Phys. Chem. Lett. **6**(1), 66–71 (2015).

15. Y. J. Jiang, M. A. Green, R. Sheng, and A. Ho-Baillie, "Room temperature optical properties of organic–inorganic lead halide perovskites," Sol. Energy Mater. Sol. Cells **137**, 253–257 (2015).

16. M. S. Alias, I. Dursun, M. I. Saidaminov, E. M. Diallo, P. Mishra, T. K. N. G. O, M. Bakr, and B. S. Ooi, "Optical constants of CH$_3$NH$_3$PbBr$_3$ perovskite thin films measured by spectroscopic ellipsometry," Opt. Express **24**(15), 16586–16594 (2016).

17. S. Brittman and E. C. Garnett, "Measuring n and k at the microscale in single crystals of CH$_3$NH$_3$PbBr$_3$ perovskite," J. Phys. Chem. C **120**(1), 616–620 (2016).

18. C. W. Chen, S. Y. Hsiao, C. Y. Chen, H. W. Kang, Z. Y. Huang, and H. W. Lin, "Optical properties of organometal halide perovskite thin films and general device structure design rules for perovskite single and tandem solar cells," J. Mater. Chem. A **3**(17), 9152–9159 (2015).

19. M. L. Zhao, Y. J. Shi, J. Dai, and J. Lian, "Ellipsometric study of the complex optical constants of a CsPbBr$_3$ perovskite thin film," J. Mater. Chem. C **6**(39), 10450–10455 (2018).

20. W. S. Yan, Y. Guo, D. Beri, S. Dottermusch, H. N. Chen, and B. S. Richards, "Experimental determination of complex optical constants of air-stable inorganic CsPbI$_3$ perovskite thin films," *Phys. Status Solidi RRL,* 2000070 (2020).

21. W. S. Yan, Y. Huang, L. Wang, F. Vüllers, M. N. Kavalenka, H. Hölscher, S. Dottermusch, B. Richards, and E. Klampaftis, "Photocurrent enhancement for ultrathin crystalline silicon solar cells via a bioinspired polymeric nanofur film with high forward scattering," Sol. Energy Mater. Sol. Cells **186**, 105–110 (2018).

22. F. Vüllers, G. Gomard, J. B. Preinfalk, E. Klampaftis, M. Worgull, B. Richards, H. Hölscher, and M. N. Kavalenka, "Bioinspired superhydrophobic highly transmissive films for optical applications," Small **12**(44), 6144–6152 (2016).

23. R. Schmager, J. Roger, J. A. Schwenzer, F. Schackmar, T. Abzieher, M. M. Byranvand, B. A. Nejand, M. Worgull, B. S. Richards, and U. W. Paetzold, "Laminated perovskite photovoltaics: enabling novel layer combinations and device architectures," Adv. Funct. Mater. **30**(9), 1907481 (2020).

24. J. A. Woollam ellipsometry solutions, *Guide to using WVASE spectroscopic ellipsometry data acquisition and analysis software* (https://www.jawoollam.com).

25. Z. F. Shi, L. Z. Lei, Y. Li, F. Zhang, Z. Z. Ma, X. J. Li, D. Wu, T. T. Xu, Y. T. Tian, B. L. Zhang, Z. Q. Yao, and G. T. Du, "Hole-injection layer-free perovskite light-emitting diodes," ACS Appl. Mater. Interfaces **10**(38), 32289–32297 (2018).

26. Z. H. Wei, A. Perumal, R. Su, S. Sushant, J. Xing, Q. Zhang, S. T. Tan, H. V. Demir, and Q. H. Xiong, "Solution-processed highly bright and durable cesium lead halide perovskite light-emitting diodes," Nanoscale **8**(42), 18021–18026 (2016).

27. G. Q. Tong, L. K. Ono, and Y. B. Qi, "Recent progress of all-bromide inorganic perovskite solar cells," Energy Technol. (Weinheim, Ger.) **8**(4), 1900961 (2020).

28. J. M. Ball, S. D. Stranks, M. T. Hörantner, S. Hüttner, W. Zhang, E. J. W. Crossland, I. Ramirez, M. Riede, M. B. Johnston, R. H. Friend, and H. J. Snaith, "Optical properties and limiting photocurrent of thin-film perovskite solar cells," Energy Environ. Sci. **8**(2), 602–609 (2015).

29. E. D. Palik, *Handbook of Optical Constants of Solids* (Elsevier, New York, 1998).

30. M. Rubin, "Optical properties of soda lime silica glasses," Sol. Energy Mater. **12**(4), 275–288 (1985).